ACS NANO
Cite This: ACS Nano 2019, 13, 10835−10844
www.acsnano.org

ARTICLE

Intracellular Photothermal Delivery for Suspension Cells Using Sharp Nanoscale Tips in Microwells

Tianxing Man,[†] Xiongfeng Zhu,[†] Yu Ting Chow,[†] Emma R. Dawson,[§] Ximiao Wen,[†] Alexander N. Patananan,[§] Tingyi Leo Liu,[†] Chuanzhen Zhao,[¶,‡] Cong Wu,[†] Jason S. Hong,[§] Pei-Shan Chung,[#] Daniel L. Clemens,[∥] Bai-Yu Lee,[∥] Paul S. Weiss,[¶,‡,□] Michael A. Teitell,[§,#,¶,△] and Pei-Yu Chiou*[,†,#,¶]

[†]Department of Mechanical and Aerospace Engineering, University of California, Los Angeles, Los Angeles, California 90095, United States

[§]Department of Pathology and Laboratory Medicine, University of California, Los Angeles, Los Angeles, California 90095, United States

[#]Department of Bioengineering, University of California, Los Angeles, Los Angeles, California 90095, United States

[¶]California NanoSystems Institute, University of California, Los Angeles, Los Angeles, California 90095, United States

[‡]Department of Chemistry and Biochemistry, University of California, Los Angeles, Los Angeles, California 90095, United States

[∥]Division of Infectious Diseases, Department of Medicine, University of California, Los Angeles, Los Angeles, California 90095, United States

[□]Department of Materials Science and Engineering, University of California, Los Angeles, Los Angeles, California 90095, United States

[△]Molecular Biology Institute, Department of Pathology and Laboratory Medicine, Department of Pediatrics, Jonsson Comprehensive Cancer Center, Broad Center of Regenerative Medicine and Stem Cell Research, University of California, Los Angeles, Los Angeles, California 90095, United States

Supporting Information

ABSTRACT: **Efficient intracellular delivery of biomolecules into cells that grow in suspension is of great interest for biomedical research, such as for applications in cancer immunotherapy. Although tremendous effort has been expended, it remains challenging for existing transfer platforms to deliver materials efficiently into suspension cells. Here, we demonstrate a high-efficiency photothermal delivery approach for suspension cells using sharp nanoscale metal-coated tips positioned at the edge of microwells, which provide controllable membrane disruption for each cell in an array. Self-aligned microfabrication generates a uniform microwell array with three-dimensional nanoscale metallic sharp tip structures. Suspension cells self-position by gravity within each microwell in direct contact with eight sharp tips, where laser-induced cavitation bubbles generate transient pores in the cell membrane to facilitate intracellular delivery of extracellular cargo. A range of cargo sizes were tested on this platform using Ramos suspension B cells with an efficiency of >84% for Calcein green (0.6 kDa) and >45% for FITC-dextran (2000 kDa), with retained viability of >96% and a throughput of >100 000 cells delivered per minute. The bacterial enzyme β-lactamase (29 kDa) was delivered into Ramos B cells and retained its biological activity, whereas a green fluorescence protein expression plasmid was delivered into Ramos B cells with a transfection efficiency of >58%, and a viability of >89% achieved.**

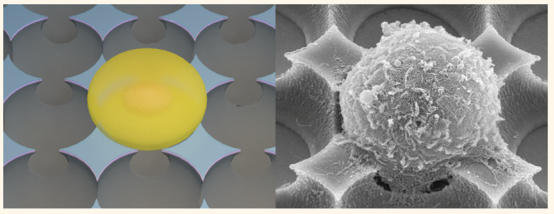

KEYWORDS: *suspension cells, photothermal delivery, self-aligned cell seeding, intracellular delivery, microwell*

High-efficiency intracellular delivery of biomolecules, including nucleic acids, proteins, and intracellular probes, is required for gene correction, immunotherapy, cellular diagnostics, and other utilities.[1−7] Suspension cells, especially lymphocytes, which represent 25−30% of

Received: July 30, 2019
Accepted: September 5, 2019
Published: September 5, 2019

DOI: 10.1021/acsnano.9b06025
ACS Nano 2019, 13, 10835−10844

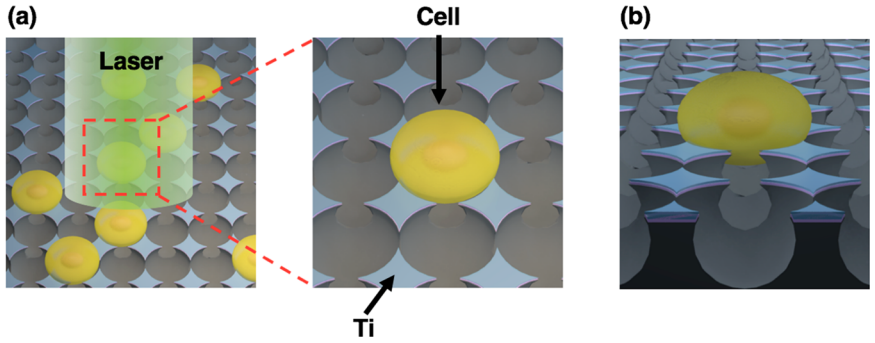

Figure 1. Photothermal delivery into suspension cells with self-aligned cell positioning. (a) Suspension cells are self-aligned within microwells by gravitational settling. Bordering metallic sharp tips at the edges of each microwell serve as local hot spots under laser irradiation to generate cavitation bubbles that open pores in adjacent, contacting cell membranes. Cargo in the surrounding medium diffuses into the cytosol of each cell through open pores on the plasma membrane. (b) Side view schematic of one cell in a microwell.

immune cells, are of great interest in cancer immunotherapies, such as CAR-T cell therapy and cancer vaccines.[8−10] However, it remains challenging to transfer cargo into suspension cells efficiently using currently available delivery methods.[11−18] Viral vectors work for delivering genetic materials into suspension cells but may induce immune responses and genotoxicity.[19−23] Nonviral vectors, including cationic polymer and lipid mixtures, show relatively low delivery efficiencies for most suspension cell types.[24−28] Physical delivery methods, such as nanoneedles, show versatility for different cell types, but are limited by scalability due to a high-precision fabrication requirement.[29−34] A carbon nanosyringe array has also been shown to be capable of delivering bioactive cargo into hard-to-transfect cells under an applied centrifugal *g*-force.[35,36] While a cell squeezing technique could deliver cargo into suspension cells with high throughput by mechanically deforming cells, the delivery efficiency and viability are dependent on cell size.[37−39] Electroporation, which can transfect suspension cells at high throughput, induces significant cell death from an applied electrical field, such as 40% cell death in suspended drop electroporation, which may not be suitable for situations with limited cell numbers.[40−45]

Recent studies deploying the photothermal effect for intracellular delivery have shown promising results.[46−55] Laser irradiation induces electron oscillations within metallic nanostructures by absorption of incident photon energy, resulting in a substantial increase in the temperature of the metal.[56,57] Heat generated by this process is rapidly transferred to a surrounding thin layer of aqueous medium where explosive cavitation bubbles nucleate.[58] The rapid expansion and collapse of cavitation bubbles exerts a large fluid shear stress on an adjacent cell membrane, which generates transient and localized pores.[59] Membrane pores generated by photothermal phenomena can be used to transport extracellular cargo into cells. The size and the number of transient pores generated in the cell membrane are critical parameters that regulate cargo delivery efficiency and cell viability. The size of cavitation bubbles can be adjusted with different laser fluences,[60] whereas the number of pores is determined by juxtaposed metallic nanostructure configurations. Gold nanoparticles have been used to create local hot spots that generate cavitation bubbles, but the number and the location of pores on each cell are not easily controlled since the nanoparticles distribute randomly in solution or on substrates.[47,48,51,54,61−65] It has been observed that high delivery efficiencies achieved by increasing nanoparticle concentration typically results in compromised cell viability in such systems.[66] To control both the size and number of transient membrane delivery pores, we investigated multiple metallic nanostructure design configurations. In our prior work, a high-precision photothermal nanoblade for large cargo delivery was developed by integrating a glass needle micropipet with a sputtered metallic tip connected to a fluid pump.[53] The cavitation bubble pattern was well controlled by the metallic structure, laser pulse strength, and pulse duration to achieve precise membrane pore opening. A massively parallel version that we termed "BLAST" was developed next to perform up to 2 μm large cargo delivery into 100 000 cells per minute with a high efficiency of 60% and cell viability of over 90%.[50]

Our current nanoblade and BLAST photothermal delivery strategies, however, face significant challenges when dealing with cells that grow in suspension. To achieve efficient membrane pore opening, direct contact between a cell and the metallic nanostructure is necessary. In contrast to adherent cells that naturally anchor on many substrate material surfaces, suspension cells are only in loose contact with substrate surfaces, including metallic nanostructures, and easily detach with slight environmental perturbations, preventing efficient biomolecule delivery. Therefore, existing flat-planar photothermal platforms are not well configured for efficient cargo delivery into suspension cells without additional adhesive materials that interfere with delivery.

Here, we demonstrate a high-efficiency photothermal delivery platform for suspension cells (Figure 1). Pore formation for cargo delivery into each cell is controlled by laser fluence and cell trapping in microwells with membrane contact to sharp, evenly spaced metallic tips. This design provides precise control over the number, location, and size of poration on suspension cells to achieve high efficiency as well as high viability. A straightforward, economical, large-area microfabrication approach generates an array of microwells with 3D nanoscale sharp tip structures. The compatibility with commercial semiconductor fabrication processes ensures the scaling capability of this platform. The sharp tips are uniformly coated with heat-conducting metal to serve as integrated local hot spots. During cell seeding, suspension cells self-position within the microwells and near sharp tip structures by gravity. Microwells of tunable dimensions physically anchor cells and ensure direct contact between cells and tips. Cavitation bubbles formed upon laser irradiation at the tips exert disruption forces on the cell membrane to generate transient pores at contact points to facilitate extracellular cargo diffusion

DOI: 10.1021/acsnano.9b06025
ACS Nano 2019, 13, 10835−10844

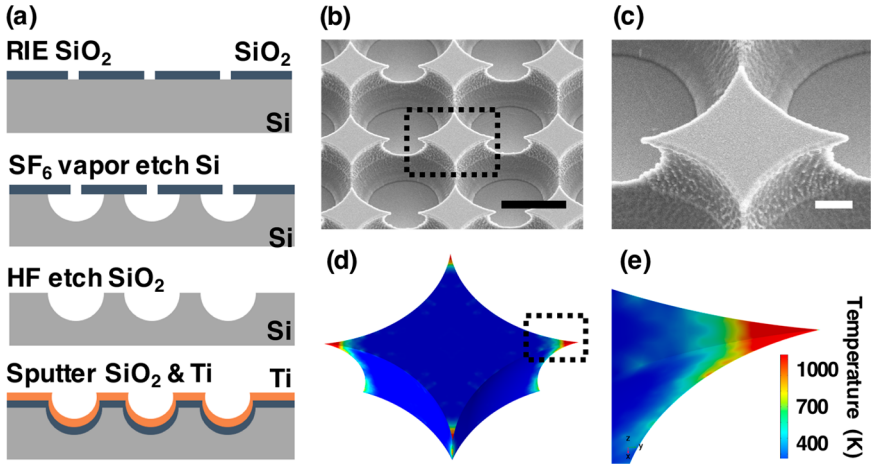

Figure 2. Fabrication, structure, and finite element simulation of microwells and sharp tips. (a) Fabrication process of microwell array and sharp tips: SiO_2 layer patterning by reactive ion etching (RIE), isotropic etching using SF_6 vapor, removal of SiO_2 by hydrogen fluoride, sputter deposition of 50 nm SiO_2 and 100 nm titanium. (b) Scanning electron microscope (SEM) image of a fabricated substrate. (c) High-magnification SEM image of the black square region in (b). (d, e) Finite element method simulation (COMSOL Multiphysics 5.3) shows the hot spots at the sharp tips. Scale bars: (b) 5 μm, (c) 1 μm.

into cells. The number of pores on each cell is predefined by eight sharp tips that surround each microwell. Pore size is determined by laser fluence, which was optimized here based on delivery results for FITC-dextran (4 kDa) into Ramos cells, a mature human B lymphocyte cell line. A range of cargo sizes was studied, with delivery efficiencies of up to 85% for Calcein green (0.6 kDa) and 45% for FITC-dextran (2000 kDa), viabilities over 98%, and throughput of greater than 100 000 cells per minute. The bacterial enzyme β-lactamase was delivered into Ramos B cells and maintained its function inside cells. A plasmid encoding green fluorescence protein (GFP) yielded a high transfection efficiency of >58% and cell viability of >89% with expression of the encoded fluorescent protein in proof-of-principle studies.

RESULTS AND DISCUSSION

Platform Design and Operating Principles. The platform substrate consists of 10^6 microwells on a 1 cm × 1 cm silicon chip with four pairs of metallic sharp tips spaced 90° from each other surrounding each microwell (Figure 1). Ramos B cells added onto the chip settle by gravity for 20 min, with self-alignment and positioning of most cells into the microwells over that time.[67] The diameter of each microwell is predesigned to fit the average cell size of interest, which is a tunable fabrication feature for different cell sizes. To ensure tip contact with a cell, the microwells are slightly smaller than the average cell size, so that size variations between cells can be mitigated. A laser beam with a 3 mm diameter scans the chip surface by manually moving an X−Y stage in steps of 1 mm, and the laser pulse was manually triggered after each step to provide one shot irradiation for every movement. To cover the entire sample, 100 pulses were fired, and the entire process requires less than 2 min by manually moving the platform. With an automatic 2D scanning mirror integrated, it takes 10 s to cover the entire sample with a 10 Hz repetition rate pulse laser used in this experiment. Metallic 3D sharp tips harvest incident laser energy and superheat the adjacent liquid to produce explosive cavitation bubbles that disrupt the membranes of cells in contact with the tips. Transient pores are generated on the cell membrane to facilitate extracellular cargo diffusion into each opened cell's cytosol before membrane repair and resealing.

A high-throughput, large-area, self-aligned fabrication process was developed to produce the microwell platform with high uniformity and scalability (Figure 2a). Because each cell settles into an individual station, the stoichiometry of tips to cells is fixed for each cell, unlike previous nanoparticle−cell mixtures. A silicon wafer with 1.2-μm-thick thermally grown SiO_2 layer was patterned and etched by reactive ion etching (RIE). The SF_6 vapor with plasma was used to undercut the silicon isotropically, creating a hemispherical structure for each microwell. Once two adjacent hemispheres expanded and merged with each other, two 3D sharp tips automatically and reproducibly form. Each microwell merges with four adjacent microwells, resulting in eight sharp tips generated for each microwell. The top layer of SiO_2 was then removed by hydrofluoric acid, followed by sputter deposition of 50-nm-thick SiO_2 and a 100-nm-thick titanium coating layer. The sputter-deposited SiO_2 layer serves as thermal isolation between the top metal layer and the bottom silicon substrate. Titanium was chosen for its high melting temperature (1941 K), compared with other commonly used heat-conducting metals, such as gold (1337 K), and excellent substrate adhesion, which enables repeated cycles of cargo delivery on the same microwell platform. The device fabrication process requires a single photolithography step free of alignment and utilizes standard foundry-compatible lithography, material etching, and metal deposition processes, which is promising for mass production at low cost in future applications. By adjusting the silicon etching time, microwells of different sizes can be fabricated to fit different types of cells.[68]

Scanning electron microscopy (SEM) images show the shape, size, and sharp Ti-coated nanoscale tip structure for each microwell (Figure 2b,c). Ramos B cells have an average diameter of 10 μm, and the diameter of the microwell for these cells was therefore fabricated to be 8 μm. The shape of the tips can be tuned by adjusting the pitch of the SiO_2 opening of each microwell. A three-dimensional (3D) finite element simulation was performed to display the local heating effect under laser irradiation of the metallic tips (Figure 2d,e). Cavitation bubbles form when the temperature of the

DOI: 10.1021/acsnano.9b06025
ACS Nano 2019, 13, 10835−10844

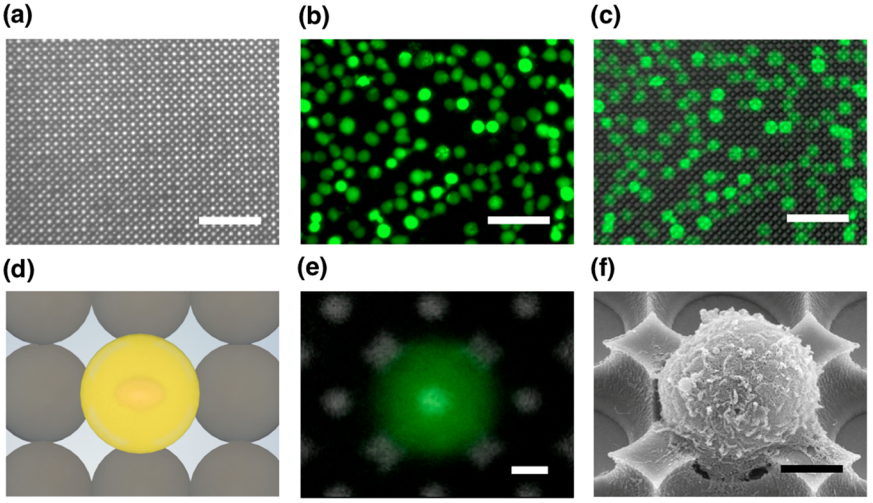

Figure 3. Self-aligned cell seeding results. (a) Bright field image of a substrate. (b) Fluorescent image of cells with Calcein AM dye stain. (c) Overlay of (a) and (b) shows alignment of cells and microwells. (d) Schematic of a cell in a microwell, (e) fluorescent image, and (f) SEM image of a paraformaldehyde-fixed cell inside a microwell. Scale bars: (a–c) 50 μm, (e, f) 3 μm.

surrounding aqueous medium rapidly rises to 80–90% of its critical temperature, which is 640–650 K for water at 1 atm.[69−73] Simulations show local heating at 1000 K, which is beyond the bubble nucleation temperature.

Gravity-Assisted Cell Positioning into Microwells. Cell positioning is critical for cargo delivery because the delivery process relies on contact between the metallic sharp tips facing each microwell and the cell membrane. Suspension cells added onto the chip and incubated for 20 min self-align with the microwells by gravity. The chip was then gently rinsed with 1× phosphate-buffered saline (PBS), pH 7.4, to remove excess cells outside of the microwells, whereas cells inside microwells remained anchored. Cells were stained with Calcein AM dye for imaging using fluorescence microscopy. A cell seeding density of 2500 cells/mm^2 was achieved over a large area, as shown in Figure S1. The gravity-assisted self-alignment of cells within microwells was shown by overlaying the bright field image of the microwells (Figure 3a) with the fluorescence image of Ramos B cells (Figure 3b) over the same area of the chip (Figure 3c). The four corner images of bright squares surrounding each microwell are the metallic sharp tips and central bright spots that show the bottom of each microwell (Figure 3d,e). To obtain a more precise image of suspension cells in the microwells, we fixed cells directly on the chip with 4% parafolmadehyde in 1× PBS, pH 7.4, after cell self-alignment and gentle washing, followed by standard cell dehydration for SEM imaging. The SEM image confirms Ramos B cells inside the microwells and sharp metallic tip to cell membrane direct contacts (Figure 3f).

Characterization of Delivery Efficiency and Cell Viability with Different Laser Fluences and Cargo Sizes. Following cell seeding into microwells, the culture medium was replaced by a solution containing the cargo for delivery. A Petri dish with the cell-positioned chip was placed on a translational X–Y stage. A Nd:YAG 6 ns pulsed laser witha wavelength of 532 nm and 3 mm diameter beam spot was set to fire at a repetition rate of 10 Hz. The laser beam was then scanned across the entire chip in 10 s by a 2D scanning mirror system. After the laser scan, the medium was changed back to regular cell culture medium for incubation.

Delivery efficiency and viability results using fluorescent molecule detection were performed 90 min after laser scanning. To count the total number of cells with fluorescence microscopy, we stained the nuclei of all cells on the chip with Hoechst 33342, a cell-permeable nucleus fluorescence dye with an emission wavelength of 497 nm. We first tested the membrane-impermeable FITC-dextran cargo with a molecular weight of 4 kDa. Control experiments were conducted by seeding cells on the microwell platform in cargo delivery solution without laser firing and scanning. No green fluorescence was detected without laser activation and scanning (Figure S2a). After laser irradiation at 21 mJ/cm^2 and whole chip scanning, over 80% of Ramos B cells showed green fluorescence staining, indicating FITC-dextran uptake. The fluorescence images of Hoechst 33342 nucleus staining (Figure 4a) and FITC-dextran delivery (Figure 4b) were overlaid to show the parallel and uniform cargo delivery across a large area of the microwell platform (Figure 4c). Co-localization of the nucleus stain and delivered FITC-dextran molecules was confirmed by overlaying high-magnification fluorescence images to show delivery results at the single-cell level (Figure 4d–f). Cell viability was evaluated using propidium iodide (PI), a red fluorescence dye that is permeable to dead cells and intercalates within the DNA in the nucleus. Images of PI staining results were obtained and overlaid with Hoechst 33342 nucleus staining and FITC-dextran green fluorescence images (Figure S2).

A range of laser fluences was tested to optimize delivery efficiency and viability. The dependence of efficiency and viability on laser fluence is shown in Figure 4g, where over 6600 cells were counted; error bars represent the standard deviation. Without laser irradiation, control experiments showed no FITC-dextran cargo delivered and 98 ± 1% cells viable. After irradiation and chip scanning at 7 mJ/cm^2 laser fluence, only 7 ± 6% of cells contained 4 kDa FITC-dextran and 98 ± 3% cells were viable. We attribute the low delivery efficiency at this fluence to suboptimal temperature increases at the sharp metallic tips, which leads to low numbers of cavitation bubbles and low numbers of pores opened on each cell membrane. When the laser fluence was increased to 14 mJ/cm^2, significantly more cavitation bubbles formed and the

DOI: 10.1021/acsnano.9b06025
ACS Nano 2019, 13, 10835–10844

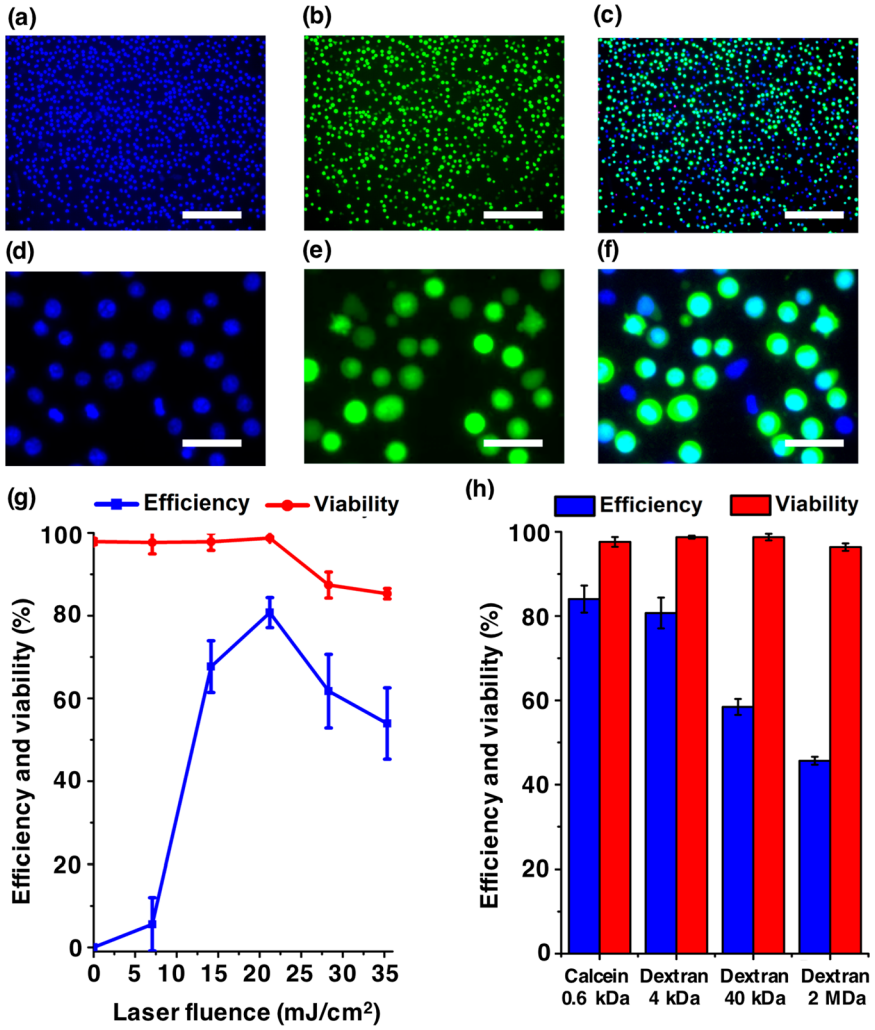

Figure 4. Quantification of delivery efficiency and cell viability under different laser fluences and cargo sizes. Large-area delivery results: (a) fluorescence image of nucleus stain (Hoechst 33342), (b) delivery of 4 kDa FITC-dextran (green), (c) overlaid image of (a) and (b) shows colocalization. (d–f) High-magnification images of fluorescence (a–c), respectively. (g) Delivery efficiency and cell viability at different laser fluences. Error bars, SD (n = 6608 cells for all tests). (h) Delivery efficiency and cell viability of cargo with sizes ranging from 0.6 to 2000 kDa (laser fluence 21 mJ/cm^2). Error bars, SD (n = 486, 3863, 3986, and 3176 for 0.6 kDa Calcein, 4 kDa FITC-dextran, 40 kDa FITC-dextran, 2000 kDa FITC-dextran, respectively). Scale bars: (a–c) 200 μm, (d–f) 40 μm.

delivery efficiency rose to 68 ± 7%. An optimum laser fluence was determined to be 21 mJ/cm^2, where a delivery efficiency of 81 ± 4% and viability of 99 ± 1% was achieved. Cell death increased after the laser fluence was raised beyond 21 mJ/cm^2. At fluences of 28 and 35 mJ/cm^2, cell viability dropped to 87 ± 3% and 85 ± 1%, respectively, as it is likely difficult for cells to recover fully from severe membrane disruption induced by excessive laser irradiation. At high fluences, delivery efficiency also falls notably, presumably because of excessive cell membrane damage and dead cells fail to retain fluorescent FITC-dextran molecules. Further, reduced photothermal effects due to damage to the metal layers of the sharp tips at high laser fluences may also account for decreases in delivery efficiencies.

Fluorescent molecules with sizes ranging from 0.6 to 2000 kDa, yielding hydrodynamic radii from <1 to 27 nm,[74] were tested to determine the accessible size delivery range of this photothermal platform configuration. Cargo solutions were prepared at the same concentration (1 mg/mL) for all types of cargo. The laser fluence was set to 21 mJ/cm^2 for the range of cargo sizes. Since cargo with higher molecular weight has a slower diffusion rate than smaller cargo, delivery efficiency drops with increasing cargo size. Overlaid images of delivered cargo with Hoechst 33342 nucleus stain and the PI dead cell biomarker are shown in Figure S3. The quantitative experimental result is shown in Figure 4h, where 480 cells, 3800 cells, 3900 cells, and 3100 cells were counted for 0.6 kDa Calcein, 4 kDa FITC-dextran, 40 kDa FITC-dextran, and 2000 kDa FITC-dextran, respectively; error bars represent standard deviations. Membrane-impermeable Calcein green of 0.6 kDa size was delivered with an efficiency of 84 ± 3%, whereas the delivery efficiency dropped to 58 ± 2% for 40 kDa FITC-dextran. For large cargo, a delivery efficiency of 46 ± 1% was achieved using 2000 kDa FITC-dextran molecules, indicating the capability of large cargo delivery using this platform. High cell viability was maintained (>96%) for different cargo sizes.

Delivery of a Functional Enzyme and Expression Plasmid into Suspension Cells. The bacterial enzyme β-lactamase (29 kDa) was delivered into Ramos cells to demonstrate the biological activity of delivered cargo. The delivery and functionality of β-lactamase were evaluated with esterified β-lactamase substrate CCF4-AM. Upon entering the

DOI: 10.1021/acsnano.9b06025
ACS Nano 2019, 13, 10835–10844

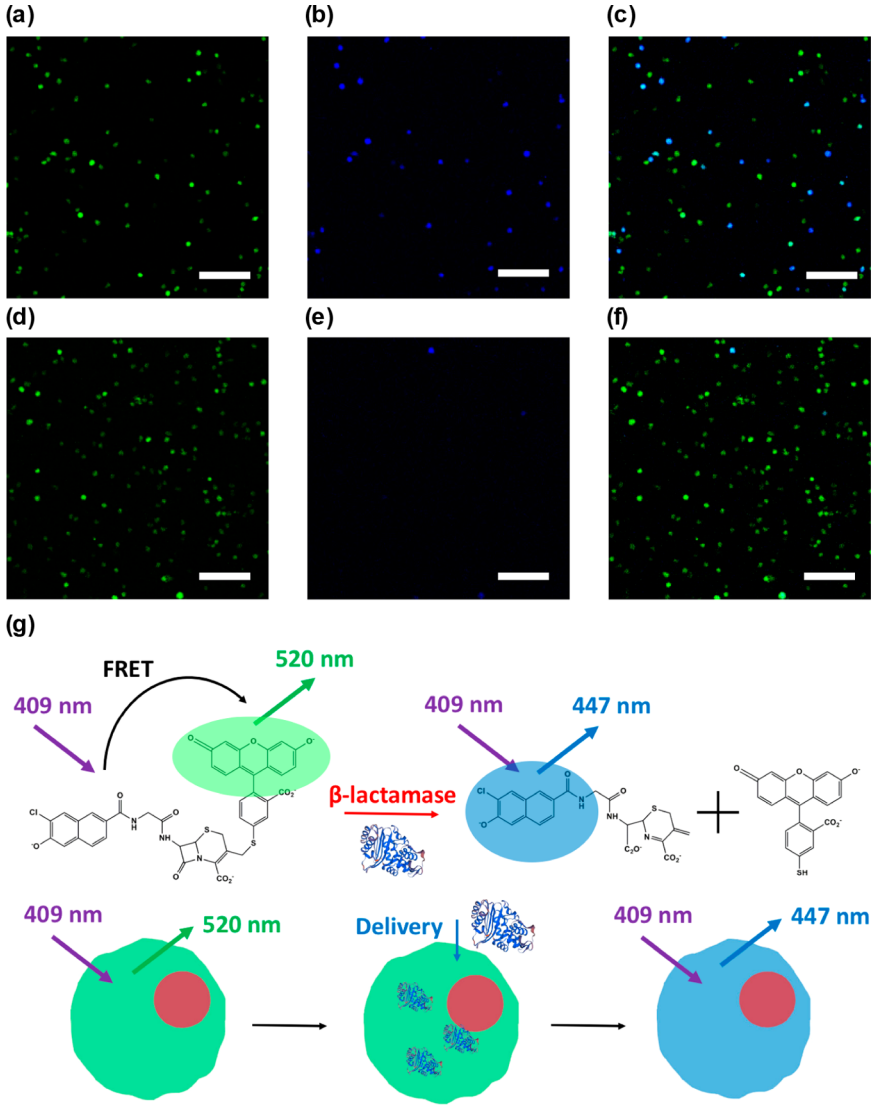

Figure 5. Bacterial enzyme β-lactamase functionality evaluated with CCF4-AM substrate. (a, d) Fluorescence images of CCF4-AM with or without laser irradiation. (b, e) β-Lactamase cleaving results with or without laser irradiation. (c, f) Overlaid images of (a) and (b), (d) and (e), respectively. (g) Mechanism of CCF4-AM substrate functionality in characterizing β-lactamase. Scale bars: (a–f) 100 μm.

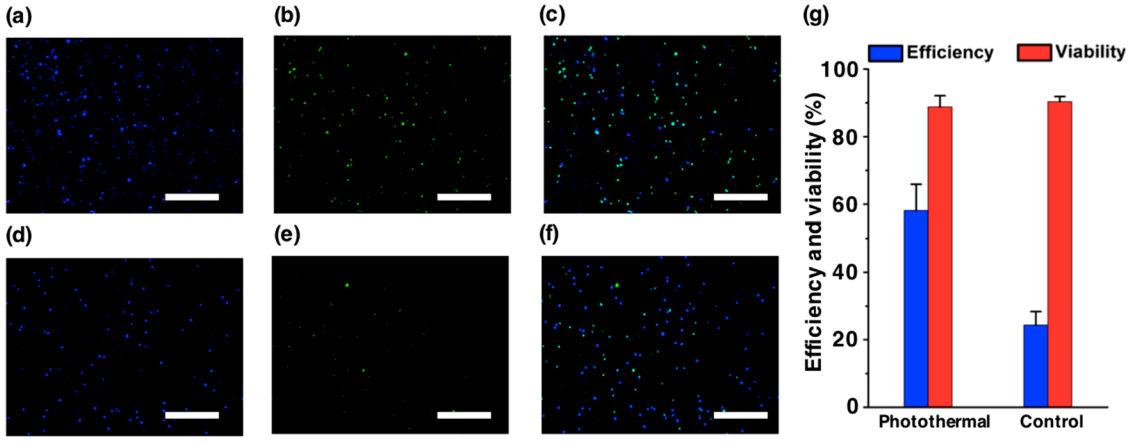

Figure 6. Green fluorescence protein (GFP) encoding plasmid transfection. Transfection results with Lipofectamine 3000 using sharp tip device: (a) fluorescence image of nucleus stain (Hoechst 33342), (b) GFP expression in Ramos cells (green), (c) overlaid image of (a) and (b) shows colocalization. Transfection results with Lipofectamine 3000 only: (d) fluorescence image of nucleus stain, (e) GFP expression in Ramos cells, (f) overlaid image of (d) and (e) shows colocalization. (g) Quantitative comparison of transfection efficiency and viability between delivery using photothermal sharp tip platform and delivery using Lipofectamine 3000 only. Scale bars: (a–f) 100 μm.

DOI: 10.1021/acsnano.9b06025
ACS Nano 2019, 13, 10835–10844

cell, CCF4-AM is converted to CCF4 by endogenous cytoplasmic esterases. CCF4 is a fluorescence resonance energy transfer (FRET) substrate, which emits green fluorescence at 520 nm with excitation at 409 nm. Once β-lactamase was delivered into cells, it cleaved CCF4 into two separate fluorophores and disrupted the FRET effect, changing the emission wavelength from 520 to 447 nm. Delivered enzyme function results are shown in Figure 5 with a 39 ± 1% substrate cleaving efficiency.

A plasmid encoding GFP was delivered into Ramos cells using the platform. The plasmid was encapsulated with Lipofectamine 3000, and the platform-activated transfection efficiency was compared to delivery with Lipofectamine only. We stained the nuclei of all cells with Hoechst 33342 to count the total number of cells. The fluorescence images of nuclei staining (Figure 6a) and GFP expression (Figure 6b) were overlaid to show colocalization (Figure 6c). A transfection efficiency of 58 ± 8% was achieved 48 h postdelivery using the sharp tip platform, compared to 24 ± 4% delivery efficiency using Lipofectamine only (Figure 6d–f), and a high cell viability of 89 ± 3% was maintained (Figure 6g).

CONCLUSIONS AND PROSPECTS

Suspension cells play essential roles in biomedicine and biomedical research, especially in areas related to the immune system. High-efficiency and high-viability suspension cell delivery approaches will enable improved applications in related fields. Here, we demonstrated a photothermal delivery platform for suspension cells with self-aligned cell positioning and controllable cell membrane delivery pores on each cell. A large-area, economical, safe, and high-throughput self-aligned device fabrication process was developed with only one etching step to create a microwell array platform with nanoscale sharp tip structures facing each microwell cavity. With cell-size designed microwells, suspension cells self-align with the microwells and tips by gravity. Metal-coated sharp tips harvest incident laser energy to generate cavitation bubbles in the surrounding medium that disrupt contacting cell membranes to create transient membrane pores for cell-impermeable cargo to diffuse into cells. The size of the cavitation bubbles, and therefore the force generated on the cell membrane and resulting pore opening size, was controlled by laser fluence, and the number of pores per cell was determined by fabricating a fixed number of tips around each cell. Delivery efficiencies of >84% for small molecules (0.6 kDa Calcein dye) and 45% for large molecules (FITC-dextran 2000 kDa) were achieved, and a cell viability of >96% was always maintained. Bacterial β-lactamase was delivered and retained biological activity inside cells. A GFP-encoded plasmid was also delivered with a high transfection efficiency of 58% and viability of 89%. The reproducible delivery of fluorescent molecules, an enzyme, and GFP-encoded plasmids shows the potential for photothermal delivery in biomedical applications for suspension cells.

Self-aligned cell seeding and anchoring by gravity enables highly efficient delivery of cargo into a large number of suspension cells nearly simultaneously. Adjusting the diameter and pitch of the platform microwells adds versatility to this platform for a wide variety of suspension cells of different sizes. The cell diameters in Figure 4b varied from 8 to 17 μm, showing the cell-to-cell size variation tolerance of the current 8 μm pitch microwell design. For biological samples that absorb visible light, the current 532 nm pulsed laser could be replaced by a near-infrared pulsed laser. Combined with the wafer-scale self-aligned fabrication process, this approach can be expanded and applied for high-efficiency, high-viability, safe, and high-throughput suspension cell intracellular delivery, which creates numerous opportunities in biomedicine.

METHODS/EXPERIMENTAL

Experimental Setup. The laser source is a Q-switched Nd:YAG laser (Minilite I, Continuum, San Jose, CA, USA), with a wavelength of 532 nm, a beam diameter of 3 mm, and a pulse duration of 6 ns. A half-wave polarizer and polarizing beam splitter designed for the 532 nm laser are used to adjust the power splitting ratio of the two beams. The laser energy was checked before every experiment using a laser energy meter (Nova II, Ophir, North Logan, UT, USA). An X–Y translation stage (Thorlabs, Newton, NJ, USA) and a 2D scanning mirror (Thorlabs) were applied to expose the entire 1 cm^2 area to the laser beam sequentially.

Temperature Simulation. We used a finite-element method (COMSOL, Multiphysics 5.3) to simulate the temperature distribution pattern. The simulation geometry was constructed according to real device dimensions in a water medium. Scattered field formulation was used to apply plane waves (wavelength = 532 nm, fluence = 21 mJ/cm^2) in the z direction. Resistive loss from electromagnetic interaction was calculated and used as the heat source for transient heat transfer. Perfectly matched layers were applied to surround the entire domain to mimic infinitely extending space.

Cell Seeding and Retrieval. Ramos *Homo sapiens* Burkitt's lymphoma B cells were obtained from ATCC (Manassas, VA, USA) and maintained in RPMI-1640 (Corning, Manassas, VA, USA) supplemented with 10% fetal bovine serum (Omega Scientific, Tarzana, CA, USA), 1% penicillin/streptomycin (Corning), 1% sodium pyruvate (Corning), and 1% nonessential amino acids (Life Technologies Corporation, Carlsbad, CA, USA). Cells were incubated at 37 °C and 5% CO_2 and were checked regularly for mycoplasma contamination using Lonza (Walkersville, MD, USA) Mycoalert mycoplasma detection kit. Cells were passaged every other day and were maintained at 5×10^5 to 2×10^6 cells/mL. The chip was put into a 35 mm Petri dish. Ramos cells were loaded into the Petri dish and kept in an incubator for 20 min to settle down when cells self-aligned with microwells and sharp tips. After incubation for 20 min, the chip was taken out and rinsed with PBS to wash away excessive cells outside microwells, while cells inside microwells remained static due to the anchoring feature of the structure. Stable seeding of 2.5×10^5 cells per chip (1 cm × 1 cm) was reproducibly achieved. It takes 2 min to scan through the chip by manual control, which yields the throughput of 1.25×10^5 cells/min. Using a 2D scanning mirror system, the scanning time reduces to 10 s. Cell-permeable dye, Calcein AM (Life Technologies Corporation), was added to stain the whole cell so as to visualize individual cells in a fluorescent microscope. Bright field images of the same area of the chip were also obtained to compare the seeding status at the single-cell level. After laser scanning, cells were retrieved by tilting the chip at 45°, gently washing out cells with culture medium, and collecting them in the Petri dish. Over 2×10^5 cells out of the 2.5×10^5 cells originally seeded in one single chip were collected. The experimental results of enzymatic function and plasmid transfection were analyzed after the cells were retrieved from the chips.

Delivery Material. Fluorescent molecules ranging from 0.6 to 2000 kDa were applied to characterize the platform. Cell-impermeable Calcein green molecules (0.6 kDa, Life Technologies Corporation) were prepared as 500 μM in PBS. FITC-dextran molecules (4, 40, and 2000 kDa, Sigma-Aldrich, St. Louis, MO, USA) were prepared as 1 mg/mL in PBS. The PBS solution containing fluorescent molecules was added into Petri dish immediately before experiments and removed by rinsing the chip three times with fresh PBS after the laser scan. The β-lactamase enzyme (Sigma-Aldrich) was dissolved in Hanks' balanced salt solution (HBSS) at 50 units/mL. MSCV-GFP plasmid (4.5 μg) was diluted in Opti-MEM (200 μL, Life Technologies Corporation) and P3000 Enhancer Reagent (9 μL, Life Technologies Corporation), mixed with Lipofectamine 3000 (12

DOI: 10.1021/acsnano.9b06025
ACS Nano 2019, 13, 10835–10844

μL, Life Technologies Corporation) in Opti-MEM (200 μL), and incubated at room temperature for 15 min.

Delivery Efficiency and Viability. Cells were stained with Hoechst 33342 (5 μg/mL, Life Technologies Corporation), a nucleus stain, to facilitate the counting of total cell number. Cells with designated cargo inside were counted as successfully delivered cells. Delivery efficiency was calculated as the number of delivered cells divided by the total number of cells. Propidium iodide (5 μg/mL, Life Technologies Corporation) was used to mark the nuclei of dead cells. Cell viability was calculated as the number of live cells (with no PI) divided by the total number of cells.

Cell Counting and Reproducibility Information. We used an automated cell-counting program in Fiji image processing software to count cells from fluorescence images. Manual checks were also performed to minimize counting errors. Each data point in Figure 4g represents the mean value of at least three randomly selected fields of view with over 100 cells counted; error bars represent standard deviations. Each data point in Figure 4h represents the mean value of at least three randomly selected fields of view with over 400 cells counted; error bars represent standard deviation. Each data point in Figure 6g represents the mean value of at least three randomly selected fields of view in three independent experiments with over 800 cells counted; error bars represent standard deviations.

Cell Fixation. Cells were fixed with 4% paraformaldehyde in PBS. After seeded on chip, cells were carefully rinsed with PBS three times and immersed in paraformaldehyde for 20 min at room temperature. Paraformaldehyde solution was fully removed with PBS rinse three times. The sample was dehydrated by soaking in ethanol of graded concentrations, which were 50% for 5 min, 70% for 5 min, 90% for 5 min, and 100% four times for 5 min each. Finally, the sample was immersed in hexamethyldisilazane three times for 7 min each and air-dried at room temperature.

Imaging. Fluorescence images were taken with an upright fluorescence microscope (Axio Scope.A1, Carl Zeiss, Jena, Germany) with a 10× objective lens. Scanning electron microscope images were obtained with a field emission scanning electron microscope (Hitachi S4700, Tokyo, Japan).

ASSOCIATED CONTENT

Supporting Information

The Supporting Information is available free of charge on the ACS Publications website at DOI: 10.1021/acsnano.9b06025.

Figures S1−S3: large-area self-aligned cell seeding results; comparison of results of 0.6 kDa Calcein delivery with and without laser scanning; delivery results of cargo of different sizes at laser fluence of 21 mJ/cm^2 (PDF)

AUTHOR INFORMATION

Corresponding Author

*E-mail: pychiou@gmail.com.

ORCID

Tianxing Man: 0000-0001-5079-3844
Chuanzhen Zhao: 0000-0003-0162-1231
Daniel L. Clemens: 0000-0003-0421-7306
Paul S. Weiss: 0000-0001-5527-6248

Author Contributions

T.M., X.Z., and P.-Y.C. conceived the idea and designed the device. T.M., X.Z., Y.T.C., and P.-Y.C. planned the experiments. T.M. fabricated the device, carried out the experiments, and analyzed the data with assistance from T.L., C.Z., C.W., J.S.H., P.-S.C., D.L.C., and B.-Y.L. T.M. and X.W. ran the numerical simulations. E.R.D. and A.N.P. prepared Ramos B cells for study. P.-Y.C., M.A.T., and P.S.W. advised on experiments, data analysis, and writing. The manuscript was written with contributions from all authors. All authors have given approval to the final version of the manuscript.

Notes

The authors declare no competing financial interest.

ACKNOWLEDGMENTS

M.A.T. and P.Y.C. were supported by NIH grant R01GM114188 and by the Air Force Office of Scientific Research grant AFOSR FA9550-15-1-0406. P.Y.C. was supported by NSF CBET 1404080. M.A.T. was supported by NIH grants R01GM073981, R01CA185189, R21CA227480, and P30CA016042. A.N.P. was supported by NIH grant T32CA009120 and AHA Award 18POST34080342. E.R.D. was supported by NIH GM55052 (CARE) and 5T34GM008563. C.Z. and P.S.W. were supported by NIH grant TR01DA045550.

REFERENCES

(1) Stewart, M. P.; Sharei, A.; Ding, X.; Sahay, G.; Langer, R.; Jensen, K. F. *In Vitro* and *ex Vivo* Strategies for Intracellular Delivery. *Nature* **2016**, *538*, 183−192.

(2) Liu, X.; Braun, G. B.; Zhong, H.; Hall, D. J.; Han, W.; Qin, M.; Zhao, C.; Wang, M.; She, Z. G.; Cao, C.; Sailor, M. J.; Stallcup, W. B.; Ruoslahti, E.; Sugahara, K. N. Tumor-Targeted Multimodal Optical Imaging with Versatile Cadmium-Free Quantum Dots. *Adv. Funct. Mater.* **2016**, *26*, 267−276.

(3) D'Astolfo, D. S.; Pagliero, R. J.; Pras, A.; Karthaus, W. R.; Clevers, H.; Prasad, V.; Lebbink, R. J.; Rehmann, H.; Geijsen, N. Efficient Intracellular Delivery of Native Proteins. *Cell* **2015**, *161*, 674−690.

(4) Zhao, C.; Bai, Z.; Liu, X.; Zhang, Y.; Zou, B.; Zhong, H. Small GSH-Capped $CuInS_2$ Quantum Dots: MPA-Assisted Aqueous Phase Transfer and Bioimaging Applications. *ACS Appl. Mater. Interfaces* **2015**, *7*, 17623−17629.

(5) Hsu, P. D.; Lander, E. S.; Zhang, F. Development and Applications of CRISPR-Cas9 for Genome Engineering. *Cell* **2014**, *157*, 1262−1278.

(6) Walsh, A. S.; Yin, H.; Erben, C. M.; Wood, M. J. A.; Turberfield, A. J. DNA Cage Delivery to Mammalian Cells. *ACS Nano* **2011**, *5*, 5427−5432.

(7) Michalet, X.; Pinaud, F. F.; Bentolila, L. A.; Tsay, J. M.; Doose, S.; Li, J. J.; Sundaresan, G.; Wu, A. M.; Gambhir, S. S.; Weiss, S. Quantum Dots for Live Cells, *in Vivo* Imaging, and Diagnostics. *Science* **2005**, *307*, 538−544.

(8) Riley, R. S.; June, C. H.; Langer, R.; Mitchell, M. J. Delivery Technologies for Cancer Immunotherapy. *Nat. Rev. Drug Discovery* **2019**, *18*, 175−196.

(9) Stankovic, B.; Bjorhovde, H. A. K.; Skarshaug, R.; Aamodt, H.; Frafjord, A.; Muller, E.; Hammarstrom, C.; Beraki, K.; Baekkevold, E. S.; Woldbaek, P. R.; Helland, A.; Brustugun, O. T.; Oynebraten, I.; Corthay, A. Immune Cell Composition in Human Non-Small Cell Lung Cancer. *Front. Immunol.* **2019**, *9*, 3101.

(10) Chan, W. C. W.; Khademhosseini, A.; Parak, W. J.; Weiss, P. S. Cancer: Approaches from Nanoscience and Technology Approaches. *ACS Nano* **2017**, *11*, 4375−4376.

(11) Rosenberg, S. A.; Restifo, N. P. Adoptive Cell Transfer as Personalized Immunotherapy for Human Cancer. *Science* **2015**, *348*, 62−68.

(12) Meir, R.; Shamalov, K.; Betzer, O.; Motiei, M.; Horovitz-Fried, M.; Yehuda, R.; Popovtzer, A.; Popovtzer, R.; Cohen, C. J. Nanomedicine for Cancer Immunotherapy: Tracking Cancer-Specific T-Cells *in Vivo* with Gold Nanoparticles and CT Imaging. *ACS Nano* **2015**, *9*, 6363−6372.

(13) Tebas, P.; Stein, D.; Tang, W. W.; Frank, I.; Wang, S. Q.; Lee, G.; Spratt, S. K.; Surosky, R. T.; Giedlin, M. A.; Nichol, G.; Holmes, M. C.; Gregory, P. D.; Ando, D. G.; Kalos, M.; Collman, R. G.; Binder-Scholl, G.; Plesa, G.; Hwang, W. T.; Levine, B. L.; June, C. H.

DOI: 10.1021/acsnano.9b06025
ACS Nano 2019, 13, 10835−10844

Gene Editing of CCR5 in Autologous CD4 T Cells of Persons Infected with HIV. *N. Engl. J. Med.* **2014**, *370*, 901−910.
(14) Peer, D. A. Daunting Task: Manipulating Leukocyte Function with RNAi. *Immunol. Rev.* **2013**, *253*, 185−197.
(15) Restifo, N. P.; Dudley, M. E.; Rosenberg, S. A. Adoptive Immunotherapy for Cancer: Harnessing the T Cell Response. *Nat. Rev. Immunol.* **2012**, *12*, 269−281.
(16) Hanahan, D.; Weinberg, R. A. Hallmarks of Cancer: The Next Generation. *Cell* **2011**, *144*, 646−674.
(17) Mellman, I.; Coukos, G.; Dranoff, G. Cancer Immunotherapy Comes of Age. *Nature* **2011**, *480*, 480−489.
(18) Waldmann, T. A. Immunotherapy: Past, Present and Future. *Nat. Med.* **2003**, *9*, 269−277.
(19) Naldini, L. Gene Therapy Returns to Centre Stage. *Nature* **2015**, *526*, 351−360.
(20) Kotterman, M. A.; Chalberg, T. W.; Schaffer, D. V. Viral Vectors for Gene Therapy: Translational and Clinical Outlook. *Annu. Rev. Biomed. Eng.* **2015**, *17*, 63−89.
(21) Nayak, S.; Herzog, R. W. Progress and Prospects: Immune Responses to Viral Vectors. *Gene Ther.* **2010**, *17*, 295−304.
(22) Thomas, C. E.; Ehrhardt, A.; Kay, M. A. Progress and Problems with the Use of Viral Vectors for Gene Therapy. *Nat. Rev. Genet.* **2003**, *4*, 346−358.
(23) Qin, X. F.; An, D. S.; Chen, I. S. Y.; Baltimore, D. Inhibiting HIV-1 Infection in Human T Cells by Lentiviral-Mediated Delivery of Small Interfering RNA against CCR5. *Proc. Natl. Acad. Sci. U. S. A.* **2003**, *100*, 183−188.
(24) Ramishetti, S.; Kedmi, R.; Goldsmith, M.; Leonard, F.; Sprague, A. G.; Godin, B.; Gozin, M.; Cullis, P. R.; Dykxhoorn, D. M.; Peer, D. Systemic Gene Silencing in Primary T Lymphocytes Using Targeted Lipid Nanoparticles. *ACS Nano* **2015**, *9*, 6706−6716.
(25) He, W.; Bennett, M. J.; Luistro, L.; Carvajal, D.; Nevins, T.; Smith, M.; Tyagi, G.; Cai, J.; Wei, X.; Lin, T. A.; Heimbrook, D. C.; Packman, K.; Boylan, J. F. Discovery of siRNA Lipid Nanoparticles to Transfect Suspension Leukemia Cells and Provide *in Vivo* Delivery Capability. *Mol. Ther.* **2014**, *22*, 359−370.
(26) Mintzer, M. A.; Simanek, E. E. Nonviral Vectors for Gene Delivery. *Chem. Rev.* **2009**, *109*, 259−302.
(27) Gresch, O.; Engel, F. B.; Nesic, D.; Tran, T. T.; England, H. M.; Hickman, E. S.; Korner, I.; Gan, L.; Chen, S.; Castro-Obregon, S.; Hammermann, R.; Wolf, J.; Muller-Hartmann, H.; Nix, M.; Siebenkotten, G.; Kraus, G.; Lun, K. New Non-Viral Method for Gene Transfer into Primary Cells. *Methods* **2004**, *33*, 151−163.
(28) McManus, M. T.; Haines, B. B.; Dillon, C. P.; Whitehurst, C. E.; van Parijs, L.; Chen, J.; Sharp, P. A. Small Interfering RNA-Mediated Gene Silencing in T Lymphocytes. *J. Immunol.* **2002**, *169*, 5754−5760.
(29) Xu, X.; Hou, S.; Wattanatorn, N.; Wang, F.; Yang, Q.; Zhao, C.; Yu, X.; Tseng, H. R.; Jonas, S. J.; Weiss, P. S. Precision-Guided Nanospears for Targeted and High-Throughput Intracellular Gene Delivery. *ACS Nano* **2018**, *12*, 4503−4511.
(30) Mitragotri, S.; Anderson, D. G.; Chen, X.; Chow, E. K.; Ho, D.; Kabanov, A. V.; Karp, J. M.; Kataoka, K.; Mirkin, C. A.; Petrosko, S. H.; Shi, J.; Stevens, M. M.; Sun, S.; Teoh, S.; Venkatraman, S. S.; Xia, Y.; Wang, S.; Gu, Z.; Xu, C. Accelerating the Translation of Nanomaterials in Biomedicine. *ACS Nano* **2015**, *9*, 6644−6654.
(31) Chiappini, C.; Martinez, J. O.; De Rosa, E.; Almeida, C. S.; Tasciotti, E.; Stevens, M. M. Biodegradable Nanoneedles for Localized Delivery of Nanoparticles *in Vivo*: Exploring the Biointerface. *ACS Nano* **2015**, *9*, 5500−5509.
(32) VanDersarl, J. J.; Xu, A. M.; Melosh, N. A. Nanostraws for Direct Fluidic Intracellular Access. *Nano Lett.* **2012**, *12*, 3881−3886.
(33) Shalek, A. K.; Gaublomme, J. T.; Wang, L.; Yosef, N.; Chevrier, N.; Andersen, M. S.; Robinson, J. T.; Pochet, N.; Neuberg, D.; Gertner, R. S.; Amit, I.; Brown, J. R.; Hacohen, N.; Regev, A.; Wu, C. J.; Park, H. Nanowire-Mediated Delivery Enables Functional Interrogation of Primary Immune Cells: Application to the Analysis of Chronic Lymphocytic Leukemia. *Nano Lett.* **2012**, *12*, 6498−6504.
(34) Cai, D.; Mataraza, J. M.; Qin, Z. H.; Huang, Z.; Huang, J.; Chiles, T. C.; Carnahan, D.; Kempa, K.; Ren, Z. Highly Efficient Molecular Delivery into Mammalian Cells Using Carbon Nanotube Spearing. *Nat. Methods* **2005**, *2*, 449−454.
(35) Choi, M.; Lee, S. H.; Kim, W. B.; Gujrati, V.; Kim, D.; Lee, J.; Kim, J. I.; Kim, H.; Saw, P. E.; Jon, S. Intracellular Delivery of Bioactive Cargos to Hard-to-Transfect Cells Using Carbon Nanosyringe Arrays under an Applied Centrifugal G-Force. *Adv. Healthcare Mater.* **2016**, *5*, 101−107.
(36) Park, S.; Kim, Y. S.; Kim, W. B.; Jon, S. Carbon Nanosyringe Array as a Platform for Intracellular Delivery. *Nano Lett.* **2009**, *9*, 1325−1329.
(37) Kollmannsperger, A.; Sharei, A.; Raulf, A.; Heilemann, M.; Langer, R.; Jensen, K. F.; Wieneke, R.; Tampe, R. Live-Cell Protein Labelling with Nanometre Precision by Cell Squeezing. *Nat. Commun.* **2016**, *7*, 10372.
(38) Han, X.; Liu, Z. B.; Jo, M. C.; Zhang, K.; Li, Y.; Zeng, Z. H.; Li, N.; Zu, Y. L.; Qin, L. D. CRISPR-Cas9 Delivery to Hard-to-Transfect Cells *Via* Membrane Deformation. *Sci. Adv.* **2015**, *1*, No. e1500454.
(39) Sharei, A.; Zoldan, J.; Adamo, A.; Sim, W. Y.; Cho, N.; Jackson, E.; Mao, S.; Schneider, S.; Han, M. J.; Lytton-Jean, A.; Basto, P. A.; Jhunjhunwala, S.; Lee, J.; Heller, D. A.; Kang, J. W.; Hartoularos, G. C.; Kim, K. S.; Anderson, D. G.; Langer, R.; Jensen, K. F. A Vector-Free Microfluidic Platform for Intracellular Delivery. *Proc. Natl. Acad. Sci. U. S. A.* **2013**, *110*, 2082−2087.
(40) Liu, C.; Zhang, L.; Liu, H.; Cheng, K. Delivery Strategies of the CRISPR-Cas9 Gene-Editing System for Therapeutic Applications. *J. Controlled Release* **2017**, *266*, 17−26.
(41) Lakshmanan, S.; Gupta, G. K.; Avci, P.; Chandran, R.; Sadasivam, M.; Jorge, A. E. S.; Hamblin, M. R. Physical Energy for Drug Delivery; Poration, Concentration and Activation. *Adv. Drug Delivery Rev.* **2014**, *71*, 98−114.
(42) Yarmush, M. L.; Golberg, A.; Sersa, G.; Kotnik, T.; Miklavcic, D. Electroporation-Based Technologies for Medicine: Principles, Applications, and Challenges. *Annu. Rev. Biomed. Eng.* **2014**, *16*, 295−320.
(43) Geng, T.; Zhan, Y.; Wang, J.; Lu, C. Transfection of Cells Using Flow-through Electroporation Based on Constant Voltage. *Nat. Protoc.* **2011**, *6*, 1192−1208.
(44) Guignet, E. G.; Meyer, T. Suspended-Drop Electroporation for High-Throughput Delivery of Biomolecules into Cells. *Nat. Methods* **2008**, *5*, 393−395.
(45) Seiffert, M.; Stilgenbauer, S.; Dohner, H.; Lichter, P. Efficient Nucleofection of Primary Human B Cells and B-CLL Cells Induces Apoptosis, which Depends on the Microenvironment and on the Structure of Transfected Nucleic Acids. *Leukemia* **2007**, *21*, 1977−1983.
(46) Saklayen, N.; Huber, M.; Madrid, M.; Nuzzo, V.; Vulis, D. I.; Shen, W.; Nelson, J.; McClelland, A. A.; Heisterkamp, A.; Mazur, E. Intracellular Delivery Using Nanosecond-Laser Excitation of Large-Area Plasmonic Substrates. *ACS Nano* **2017**, *11*, 3671−3680.
(47) Lyu, Z.; Zhou, F.; Liu, Q.; Xue, H.; Yu, Q.; Chen, H. A Universal Platform for Macromolecular Delivery into Cells Using Gold Nanoparticle Layers *Via* the Photoporation Effect. *Adv. Funct. Mater.* **2016**, *26*, 5787−5795.
(48) Li, M.; Lohmuller, T.; Feldmann, J. Optical Injection of Gold Nanoparticles into Living Cells. *Nano Lett.* **2015**, *15*, 770−775.
(49) Messina, G. C.; Dipalo, M.; La Rocca, R.; Zilio, P.; Caprettini, V.; Proietti Zaccaria, R.; Toma, A.; Tantussi, F.; Berdondini, L.; De Angelis, F. Spatially, Temporally, and Quantitatively Controlled Delivery of Broad Range of Molecules into Selected Cells through Plasmonic Nanotubes. *Adv. Mater.* **2015**, *27*, 7145−7149.
(50) Wu, Y. C.; Wu, T. H.; Clemens, D. L.; Lee, B. Y.; Wen, X.; Horwitz, M. A.; Teitell, M. A.; Chiou, P. Y. Massively Parallel Delivery of Large Cargo into Mammalian Cells with Light Pulses. *Nat. Methods* **2015**, *12*, 439−444.
(51) Xiong, R.; Raemdonck, K.; Peynshaert, K.; Lentacker, I.; De Cock, I.; Demeester, J.; De Smedt, S. C.; Skirtach, A. G.; Braeckmans, K. Comparison of Gold Nanoparticle Mediated Photoporation: Vapor

DOI: 10.1021/acsnano.9b06025
ACS Nano 2019, 13, 10835−10844

Nanobubbles Outperform Direct Heating for Delivering Macromolecules in Live Cells. *ACS Nano* **2014**, *8*, 6288−6296.
(52) Sengupta, A.; Kelly, S. C.; Dwivedi, N.; Thadhani, N.; Prausnitz, M. R. Efficient Intracellular Delivery of Molecules with High Cell Viability Using Nanosecond-Pulsed Laser-Activated Carbon Nanoparticles. *ACS Nano* **2014**, *8*, 2889−2899.
(53) Wu, T. H.; Teslaa, T.; Kalim, S.; French, C. T.; Moghadam, S.; Wall, R.; Miller, J. F.; Witte, O. N.; Teitell, M. A.; Chiou, P. Y. Photothermal Nanoblade for Large Cargo Delivery into Mammalian Cells. *Anal. Chem.* **2011**, *83*, 1321−1327.
(54) Ghosh, P.; Han, G.; De, M.; Kim, C. K.; Rotello, V. M. Gold Nanoparticles in Delivery Applications. *Adv. Drug Delivery Rev.* **2008**, *60*, 1307−1315.
(55) Dai, Q.; Wilhelm, S.; Ding, D.; Syed, A. M.; Sindhwani, S.; Zhang, Y.; Chen, Y. Y.; MacMillan, P.; Chan, W. C. W. Quantifying the Ligand-Coated Nanoparticle Delivery to Cancer Cells in Solid Tumors. *ACS Nano* **2018**, *12*, 8423−8435.
(56) Furlani, E. P.; Karampelas, I. H.; Xie, Q. Analysis of Pulsed Laser Plasmon-Assisted Photothermal Heating and Bubble Generation at the Nanoscale. *Lab Chip* **2012**, *12*, 3707−3719.
(57) Boulais, E.; Lachaine, R.; Meunier, M. Plasma Mediated Off-Resonance Plasmonic Enhanced Ultrafast Laser-Induced Nanocavitation. *Nano Lett.* **2012**, *12*, 4763−4769.
(58) Lukianova-Hleb, E.; Hu, Y.; Latterini, L.; Tarpani, L.; Lee, S.; Drezek, R. A.; Hafner, J. H.; Lapotko, D. O. Plasmonic Nanobubbles as Transient Vapor Nanobubbles Generated around Plasmonic Nanoparticles. *ACS Nano* **2010**, *4*, 2109−2123.
(59) Prentice, P.; Cuschierp, A.; Dholakia, K.; Prausnitz, M.; Campbell, P. Membrane Disruption by Optically Controlled Microbubble Cavitation. *Nat. Phys.* **2005**, *1*, 107−110.
(60) Kotaidis, V.; Dahmen, C.; von Plessen, G.; Springer, F.; Plech, A. Excitation of Nanoscale Vapor Bubbles at the Surface of Gold Nanoparticles in Water. *J. Chem. Phys.* **2006**, *124*, 184702.
(61) Morales, D. P.; Morgan, E. N.; McAdams, M.; Chron, A. B.; Shin, J. E.; Zasadzinski, J. A.; Reich, N. O. Light-Triggered Genome Editing: Cre Recombinase Mediated Gene Editing with Near-Infrared Light. *Small* **2018**, *14*, No. e1800543.
(62) Chen, J.; Guo, Z.; Tian, H.; Chen, X. Production and Clinical Development of Nanoparticles for Gene Delivery. *Mol. Ther.–Methods Clin. Dev.* **2016**, *3*, 16023.
(63) Morales, D. P.; Braun, G. B.; Pallaoro, A.; Chen, R.; Huang, X.; Zasadzinski, J. A.; Reich, N. O. Targeted Intracellular Delivery of Proteins with Spatial and Temporal Control. *Mol. Pharmaceutics* **2015**, *12*, 600−609.
(64) Huang, X.; Pallaoro, A.; Braun, G. B.; Morales, D. P.; Ogunyankin, M. O.; Zasadzinski, J.; Reich, N. O. Modular Plasmonic Nanocarriers for Efficient and Targeted Delivery of Cancer-Therapeutic siRNA. *Nano Lett.* **2014**, *14*, 2046−2051.
(65) Lukianova-Hleb, E. Y.; Mutonga, M. B.; Lapotko, D. O. Cell-Specific Multifunctional Processing of Heterogeneous Cell Systems in a Single Laser Pulse Treatment. *ACS Nano* **2012**, *6*, 10973−10981.
(66) Pitsillides, C. M.; Joe, E. K.; Wei, X.; Anderson, R. R.; Lin, C. P. Selective Cell Targeting with Light-Absorbing Microparticles and Nanoparticles. *Biophys. J.* **2003**, *84*, 4023−4032.
(67) Rettig, J. R.; Folch, A. Large-Scale Single-Cell Trapping and Imaging Using Microwell Arrays. *Anal. Chem.* **2005**, *77*, 5628−5634.
(68) Xu, X.; Yang, Q.; Wattanatorn, N.; Zhao, C.; Chiang, N.; Jonas, S. J.; Weiss, P. S. Multiple-Patterning Nanosphere Lithography for Fabricating Periodic Three-Dimensional Hierarchical Nanostructures. *ACS Nano* **2017**, *11*, 10384−10391.
(69) Lachaine, R.; Boulais, E.; Meunier, M. From Thermo- to Plasma-Mediated Ultrafast Laser-Induced Plasmonic Nanobubbles. *ACS Photonics* **2014**, *1*, 331−336.
(70) Hogan, N. J.; Urban, A. S.; Ayala-Orozco, C.; Pimpinelli, A.; Nordlander, P.; Halas, N. J. Nanoparticles Heat through Light Localization. *Nano Lett.* **2014**, *14*, 4640−4645.
(71) Neumann, O.; Urban, A. S.; Day, J.; Lal, S.; Nordlander, P.; Halas, N. J. Solar Vapor Generation Enabled by Nanoparticles. *ACS Nano* **2013**, *7*, 42−49.
(72) Fang, Z.; Zhen, Y. R.; Neumann, O.; Polman, A.; García de Abajo, F. J.; Nordlander, P.; Halas, N. J. Evolution of Light-Induced Vapor Generation at a Liquid-Immersed Metallic Nanoparticle. *Nano Lett.* **2013**, *13*, 1736−1742.
(73) Sassaroli, E.; Li, K. C. P.; O'Neill, B. E. Numerical Investigation of Heating of a Gold Nanoparticle and the Surrounding Microenvironment by Nanosecond Laser Pulses for Nanomedicine Applications. *Phys. Med. Biol.* **2009**, *54*, 5541−5560.
(74) Armstrong, J. K.; Wenby, R. B.; Meiselman, H. J.; Fisher, T. C. The Hydrodynamic Radii of Macromolecules and Their Effect on Red Blood Cell Aggregation. *Biophys. J.* **2004**, *87*, 4259−4270.

DOI: 10.1021/acsnano.9b06025
ACS Nano 2019, 13, 10835−10844